FEATURE ARTICLE

Structure and Electronic Properties of Carbon Nanotubes

Teri Wang Odom, Jin-Lin Huang, Philip Kim, and Charles M. Lieber*

Department of Chemistry and Chemical Biology and Division of Engineering and Applied Sciences, Harvard University, Cambridge, Massachusetts 02138

Received: October 7, 1999; In Final Form: January 6, 2000

Scanning tunneling microscopy, spectroscopy, and tight-binding calculations have been used to elucidate the unique structural and electronic properties of single-walled carbon nanotubes (SWNTs). First, the unique relationship between SWNT atomic structure and electronic properties, and the richness of structures observed in both purified and chemically etched nanotube samples are discussed. Second, a more detailed picture of SWNT electronic band structure is developed and compared with experimental tunneling spectroscopy measurements. Third, experimental and theoretical investigations of localized structures, such as bends and ends in nanotubes, are presented. Last, quantum size effects in nanotubes with lengths approaching large molecules are discussed. The implications of these studies and important future directions are considered.

Introduction

Carbon nanotubes are currently the focus of intense interest worldwide. This attention to carbon nanotubes is not surprising in light of their promise to exhibit unique physical properties that could impact broad areas of science and technology, ranging from super strong composites to nanoelectronics.[1−3] Recent experimental studies have shown that carbon nanotubes are the stiffest known material[4,5] and buckle elastically (vs fracture) under large bending or compressive strains.[5,6] These mechanical characteristics demonstrate clearly that nanotubes have significant potential for advanced composites. We believe, however, it is the remarkable electronic properties of carbon nanotubes that offer the greatest intellectual challenges and potential for novel applications. For example, theoretical calculations first predicted that single-walled carbon nanotubes (SWNTs) could exhibit either metallic or semiconducting behavior depending only on diameter and helicity.[7−9] This ability to display fundamentally distinct electronic properties without changing the local bonding, which was recently experimentally demonstrated through atomically resolved scanning tunneling microscopy (STM) measurements,[10,11] sets nanotubes apart from all other nanowire materials.[12,13]

SWNTs can be viewed as an extension in one-dimension (1D) of different fullerene molecular clusters or as a strip cut from an infinite graphene sheet and rolled up to form a tube (Figure 1a). Major characteristics of their electronic properties can be built up from relatively simply Hückel-type models using p(π) atomic orbitals. The diameter and helicity of a SWNT are uniquely characterized by the roll-up vector $\mathbf{C}_h = n\mathbf{a}_1 + m\mathbf{a}_2 \equiv (n,m)$ that connects crystallographically equivalent sites on a two-dimensional (2D) graphene sheet, where $\mathbf{a}_1$ and $\mathbf{a}_2$ are the graphene lattice vectors and n and m are integers. The limiting, achiral cases, (n,0) zigzag, and (n,n) armchair are indicated with dashed lines in Figure 1b. The translation vector **T** is along the tube axis and orthogonal to $\mathbf{C}_h$, and its magnitude represents the length of the unit cell of an (n,m) tube. The rolled-up area swept out by **T** and $\mathbf{C}_h$ (Figure 1b, gray) corresponds to the repeat unit of an (n,m) tube; hence, a nanotube's (n,m) symmetry determines the size of its unit cell, which can vary greatly among tubes.

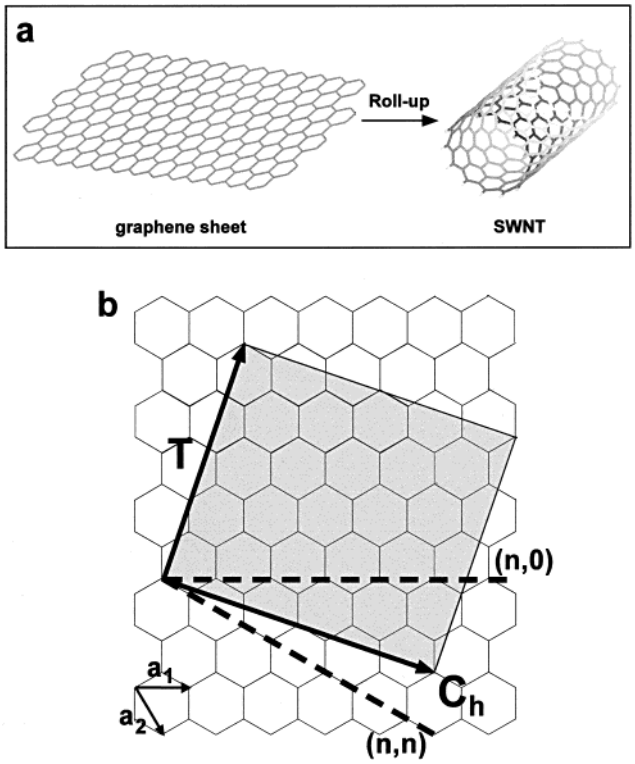

Figure 1. Schematic of a 2D graphene sheet illustrating lattice vectors $\mathbf{a}_1$ and $\mathbf{a}_2$, and the roll-up vector $\mathbf{C}_h = n\mathbf{a}_1 + m\mathbf{a}_2$. The limiting, achiral cases of (n,0) zigzag and (n,n) armchair are indicated with dashed lines. The translation vector **T** is along the nanotube axis and defines the 1D unit cell. The shaded, boxed area represents the unrolled unit cell formed by **T** and $\mathbf{C}_h$. The diagram is constructed for (n,m) = (4,2).

Electronic band structure calculations predict that the (n,m) indices determine whether a SWNT will be a metal or a semiconductor.[7−9] To understand this unique ability to exhibit distinct electronic properties within an all-carbon sp^2 hybridized

10.1021/jp993592k CCC: $19.00
Published on Web 02/15/2000

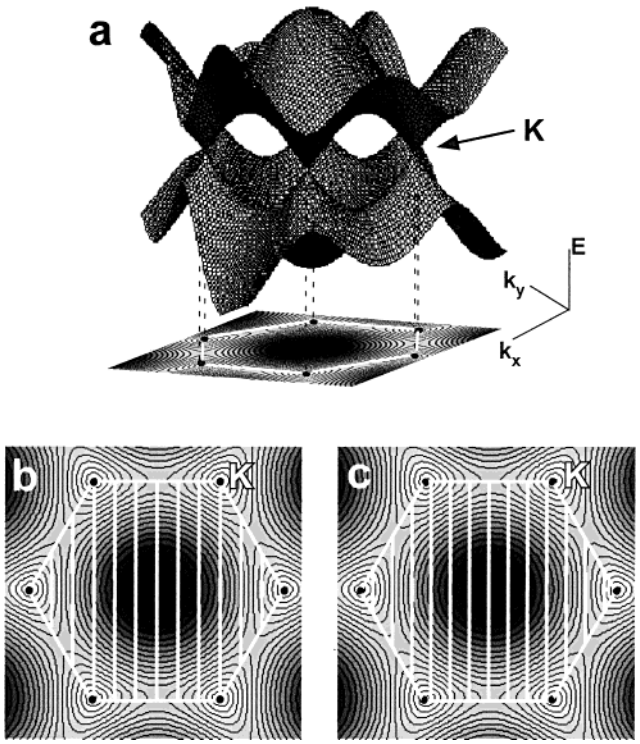

Figure 2. (a) Three-dimensional view of the graphene π/π^* bands and its 2D projection. (b) Example of the allowed 1D subbands for a metallic tube. Schematic depicts (9,0). (c) Example of the quantized 1D subbands for a semiconducting tube. Schematic shows (10,0). The white hexagon defines the first Brilluion zone of graphene, and the black dots in the corners are the graphene **K** points.

network, it is instructive to consider the 2D energy dispersion of graphite. Graphite is a semi-metal or zero-gap semiconductor whose valence and conduction bands touch and are degenerate at six **K** (k_F) points; these six positions define the corners of the first Brilluion zone (Figure 2a). As a finite piece of the 2D graphene sheet is rolled up to form a 1D tube, the periodic boundary conditions imposed by $\mathbf{C}_h$ can be used to enumerate the allowed 1D subbands, the quantized states resulting from radial confinement, as follows:

$$\mathbf{C}_h \bullet \mathbf{k} = 2\pi q \quad (1)$$

where q is an integer. If one of these allowed subbands passes through one of the K points, the nanotube will be metallic and otherwise semiconducting. As demonstrative examples, Figures 2b and 2c show the allowed subbands for two zigzag tubes, (9,0) and (10,0), respectively. Notice that the (9,0) subbands contain a K point while none of the (10,0) subbands do. The condition for metallic tubes is

$$\mathbf{C}_h \bullet \mathbf{k_F} = 2\pi q \quad (2)$$

Thus to first order, zigzag (n,0) or chiral (n,m) SWNTs are metallic when $(n - m)/3$ is an integer and otherwise semiconducting.

Independent of helicity, the energy gaps of the semiconducting (n,0) and (n,m) tubes should depend inversely on diameter. This inverse dependence of the energy gap on diameter can be understood qualitatively as follows: The semiconducting energy gap corresponds to the vertical separation between π and π^* bands at the same k position of the 1D subband closest to **K** (Figures 2a and 2c). Because the separation of 1D subbands is inversely proportional to diameter, larger semiconducting tubes will have an allowed state closer to **K** and have a correspondingly smaller energy gap. In addition, the finite curvature of the tubes also leads to mixing of the π/σ bonding and π^*/σ^* antibonding orbitals on carbon. This mixing should cause the graphene band crossing (k_F) to shift away from the **K** point and should produce small gaps in (n,0) and (n,m) metallic tubes with the magnitude of the gap depending inversely on the square of the diameter.[7,14] However, (n,n) armchair tubes are expected to be truly metallic since k_F remains on the subband of the nanotube.[15]

Scanning tunneling microscopy and spectroscopy (STS) offer the potential to probe these predictions about the electronic properties of carbon nanotubes, since these techniques are capable of resolving simultaneously the atomic structure and electronic density of states of a material. In this Feature Article, we will describe a broad range of studies drawn primarily from the authors' laboratory addressing the unique electronic properties of SWNTs. First, we will discuss the relationship between atomic structure and electronic properties and comment on the richness of structures observed in both purified and chemically etched nanotube samples. Second, we address in more detail SWNT electronic band structure with a comparison of tunneling spectroscopy measurements and tight-binding calculations. Third, we depart from the intrinsic electronic properties of perfect structures and describe experimental and theoretical investigations of localized structures such as bends and ends in nanotubes. Fourth, we discuss quantum size effects in nanotubes with lengths as small as three nanometers. Last, we conclude with a brief summary and prospects for future studies of these materials.

General Experimental Methods

Sample Preparation and STM Imaging. SWNTs were grown by laser vaporization and purified using published methods.[16,17] Samples suitable for STM studies were prepared by spin coating nanotube suspensions of dichloroethane onto Au(111) surfaces.[11,18] To ensure reasonable nanotube dispersion on the substrate ($\sim$1 μm separation between ropes), test samples were prepared and imaged by atomic force microscopy prior to insertion in the STM. STM imaging studies were carried out in our home-built, low temperature, ultrahigh vacuum (UHV) STM using electrochemically etched W tips in the constant current mode with the bias voltage (V) applied to the tip. The resolution and calibration of the STM were confirmed in-situ by imaging of the atomic lattice and steps of the Au (111) substrate surface. A typical large-scale STM image of individual tubes and small ropes containing a number of individual SWNTs is shown in Figure 3a.

Spectroscopic Characterization. STS measurements were made by averaging 5−10 current vs voltage (I−V) curves at specified locations on atomically resolved SWNTs. Typically, 6−8 distinct locations were measured for a given atomically resolved nanotube. The normalized conductance, $(V/I)dI/dV$, which has been shown to provide a good measure of major features in the local density of electronic states (LDOS) for metals and semiconductors,[19] was calculated from digital I−V data using standard methods.[11,18,19] I−V data recorded from individual SWNTs and small ropes often showed small shifts of 0.1−0.3 V, while larger ropes typically exhibited no shifts. These shifts may be due to charge transfer from the substrate. To ensure the reliability of these measurements we routinely checked that clean areas of the Au(111) substrate exhibited characteristic metallic I−V curves and the expected 2D surface state[20] of this material. In addition, we routinely checked that I varied exponentially with tip−sample separation to verify the presence of a clean vacuum tunneling junction.

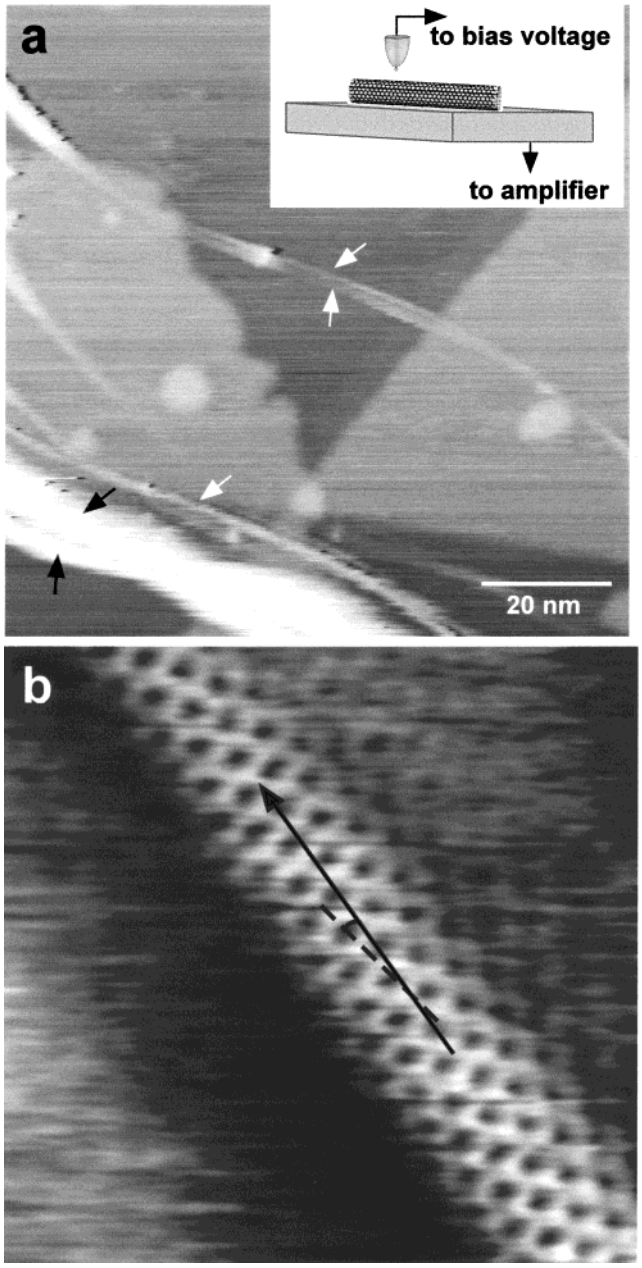

Figure 3. (a) Large area STM image showing several small bundles and isolated SWNTs on a stepped Au(111) surface. The white arrows indicate individual SWNTs and the black arrows point to small ropes of SWNTs. (inset) Schematic diagram of the STM experiment. (b) STM image of a SWNT on the surface of a rope. The solid, black arrow highlights the tube axis and the dashed line indicates the zigzag direction. The image was recorded in the constant current mode with a bias voltage of 50 mV and a tunneling current of 0.15 nA. Adapted from ref 11.

Diameter and Angle Characterization. The (*n*,*m*) indices of a SWNT are obtained from the experimentally determined values of the chiral angle, θ, and diameter *d*. The chiral angle was measured between the zigzag (n,0) direction, which corresponds to sites separated by 0.426 nm, and the central tube axis. Because the tube axis vector **T** is perpendicular to $\mathbf{C}_h$, this angle is equivalent to that between the (n,0) and $\mathbf{C}_h$ directions defined in Figure 1b. In Figure 3b, a dashed line indicates the zigzag direction, and the solid line with an arrow indicates the tube axis. This approach confines our angle measurements to the best defined atomic structure at the tops of the SWNTs and minimizes contributions from the structure at the sides of the highly curved tubes, since the latter can be distorted by the finite size and asymmetry of the tip. SWNT chiral angles and diameters were also determined from the projected nanotube images after deconvoluting the tip contribution to the image. This deconvolution process is described in more detail elsewhere.[18] We believe that this approach yields a better estimated diameter than that determined from the apparent nanotube height, since the apparent height results from the combination of both electronic properties and topography of the sample, and thus is highly dependent on the imaging (i.e., bias voltage) conditions.

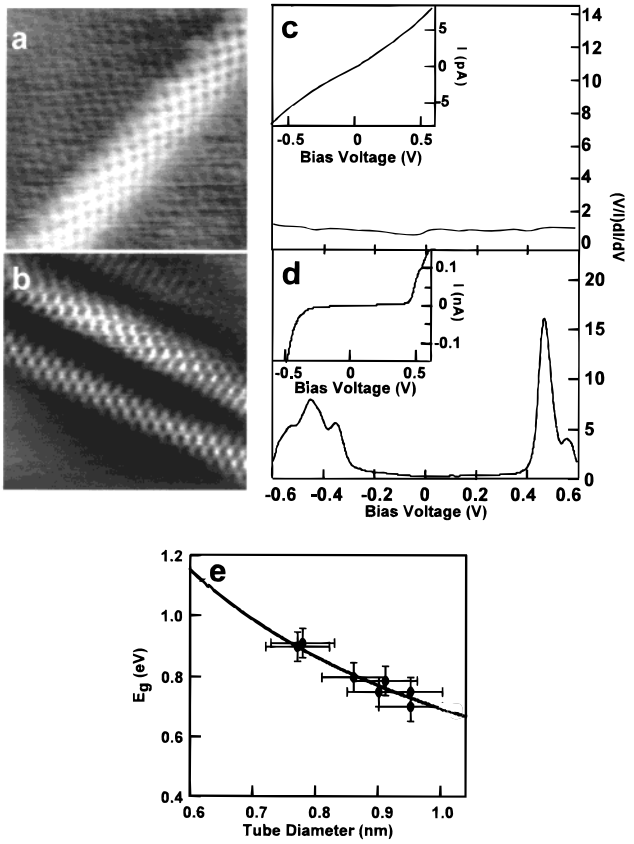

Figure 4. (a,b) Constant current images of isolated SWNTs on a Au (111) surface recorded with bias voltages of 100 and 300 mV, respectively. The Au (111) lattice is clearly seen in (a). (c,d) Calculated normalized conductance, $(V/I)dI/dV$ and measured I−V (inset) recorded on the nanotubes in a,b. (e) Summary of energy gap (E_g) versus tube diameter obtained in these studies. The solid line corresponds to a fit described in the text.

Atomic Structure and Electronic Properties of SWNTs

Typical atomically resolved images of isolated SWNTs on a Au (111) substrate are shown in Figures 4a and 4b. The high-resolution images of the nanotubes exhibit a graphene-like honeycomb lattice which enables us to define the (n,m) indices from these images. The measured chiral angle and diameter of the tube in Figure 4a constrain the (n,m) indices to either (12,3) or (13,3). Note that a (12,3) tube is expected to be metallic, while a (13,3) tube should be semiconducting. On the other hand, the chiral angle and diameter of the SWNT in Figure 4b constrain the indices to (14,−3). This tube has chirality opposite the SWNT in Figure 4a.

The ability to characterize the electronic properties of the atomically resolved tubes by tunneling spectroscopy has enabled us to determine whether the electronic properties depend on structure. Tunneling current versus voltage data recorded along the two tubes discussed above exhibit very different character-

istics (Figures 4c and 4d), and the LDOS that is determined from these I−V data sets are quite distinct. For the tube we assigned as (12,3) or (13,3), the LDOS is finite and constant between −0.6 and +0.6 V. This behavior is characteristic of a metal, and thus shows that the (12,3) indices provide the best description for the tube. Moreover, the normalized conductance data determined for the (14,−3) tube exhibit an absence of electronic states at low energies but sharp increases in the LDOS at −0.325 and +0.425 V. These sharp increases are characteristic of the conduction and valence bands of a semiconductor, and thus confirm our expectation that (14,−3) indices correspond to a semiconducting SWNT. These key measurements first verified the unique ability of SWNTs to exhibit fundamentally different electronic properties with only subtle variations in structure.[10,11]

In addition, we have characterized similar semiconducting behavior for other chiral and zigzag tubes characterized with atomic resolution. A summary of the energy gaps (E_g) obtained from these measurements is shown in Figure 4e. Significantly, these results show the expected $1/d$ dependence described in the Introduction. Moreover, these results can be used to obtain a value for the nearest neighbor overlap integral (γ_o) used in tight-binding calculations of the electronic properties by fitting to $E_g = 2\gamma_o a_{C-C}/d$, where a_{C-C} is 0.142 nm. The value obtained from the one-parameter fit, 2.5 eV, is in good agreement with the reported values in the literature that range from 2.4 to 2.9 eV.[1,21,22] Importantly, we can use this value of γ_o in tight-binding calculations to explore self-consistently the overall electronic band structure of SWNTs (see below).

Structural Statistics and Chemical Etching Effects of SWNTs

Compilation of our data on purified nanotubes results in a richness of structures statistically favoring helicities closer to the zigzag (n,0) direction rather than the armchair (n,n) direction. This observation contrasted initial suggestions that SWNTs prepared by laser vaporization consist primarily of (10,10) armchair tubes,[23] and shows clearly the importance of measurements on individual structures vs bulk samples when elucidating intrinsic properties of heterogeneous materials. STM measurements are, however, biased toward SWNTs that have been separated from outer portions of ropes. To investigate differences in structural diversity between the inner and outer portions of ropes, which might result from specific growth mechanisms, we have subjected purified SWNTs to chemical etching.[24] A schematic of the effects of chemical etching on the tubes is indicated in Figure 5a. The etching process reduces the length of the nanotube ropes and reduces the cross-sectional diameter of the ropes. AFM and STM characterization of these solutions indicates that the nanotubes are indeed shorter. However, an STM image of these etched nanotubes shows their tendency to aggregate to form "super" ropes in order to minimize the newly exposed surfaces (Figure 5b). Although this procedure fails to produce isolated single tubes, we are still able to investigate whether the cutting and etching process produces changes in the helicity of the nanotube sample.

STM experiments were performed on a series of etched samples and these statistics are compared with purified samples. Figure 5c shows the combined results obtained from ∼125 characterized nanotubes. While it appears that unetched samples exhibit structures statistically favoring helicities closer to the zigzag (n,0) direction, the etched samples indicate a shift toward the armchair (n,n) direction. Further etching of this etched sample results in a more uniform distribution of helicities. The trend toward a statistically even distribution of chiral angles is reasonable since no one structure is expected to dominate in nanotube samples grown by the laser vaporization method at high temperature.

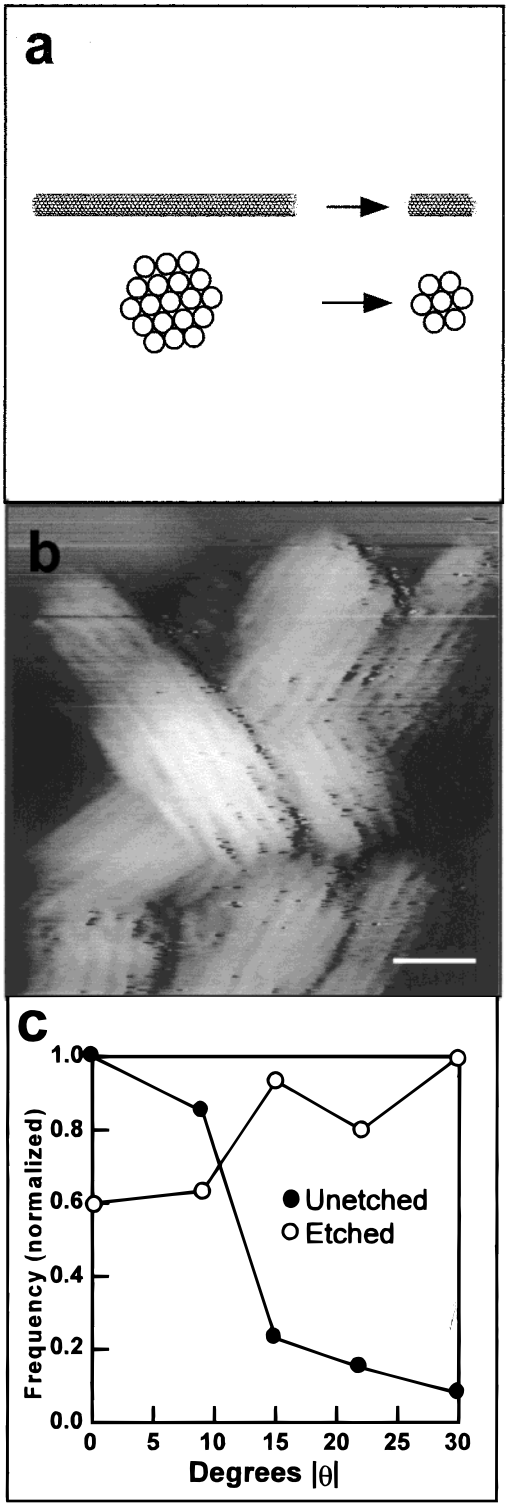

Figure 5. (a) Schematic process of chemical etching effects on SWNTs viewed from the side and end-on. (b) STM image of overlapping "super-ropes" which often aggregate together after the etching process. The scale bar is 10 nm. (c) Statistical results on the chirality of SWNTs before etching and after etching. Over 125 tubes are represented in this graph.

Structure within SWNT Ropes. To maximize van der Waals contact and lower their free energy, individual SWNTs align themselves with each other to form ropes. Transmission electron

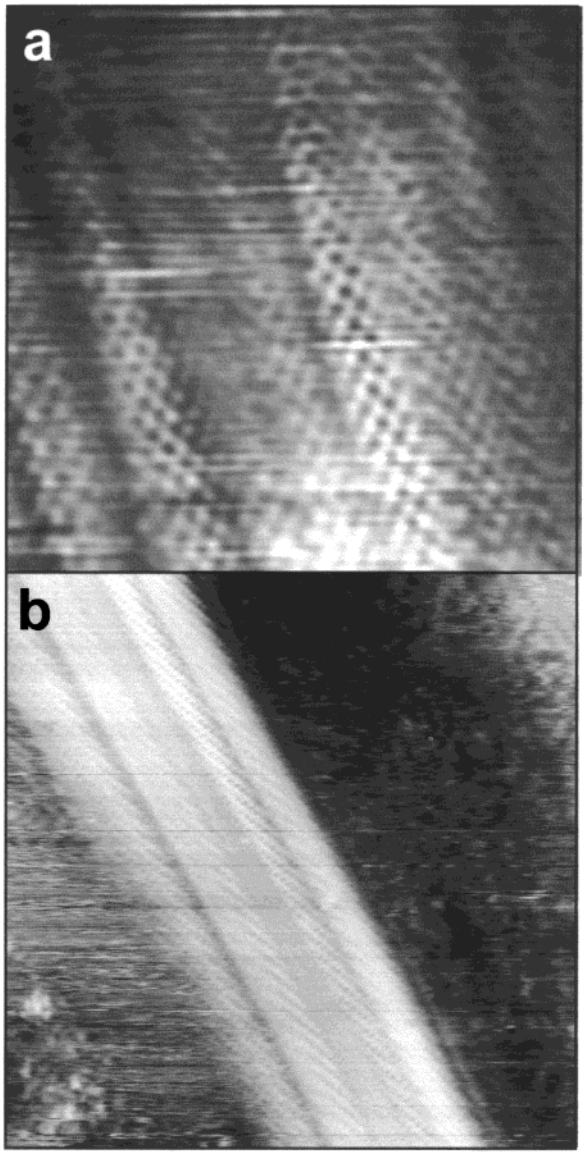

Figure 6. STM images of ropes whose individual tubes exhibit similar helicities. If one looks at the glancing angle across the tubes' atomic lattice, the similarities in helicity are readily apparent. (a) STM image of a zigzag-like rope. (b) STM image of a "raft-like" rope.

microscopy images have shown that individual nanotubes are aligned parallel to each other within a rope, and, when viewed end-on, the nanotubes pack together in a hexagonal lattice.[17] In our STM studies, we have found that if the nanotubes comprising the rope are well aligned and packed closely together, they often exhibit helicities similar to each other. STM images of several examples are shown in Figure 6. These same-helicity structures have also been observed for larger diameter tubes within ropes.[25] This observation is not unexpected due to the increased van der Waals interaction that can arise in lattice-matched structures and ropes[24,26] and may offer insight into the unresolved growth mechanism of tubes produced by laser vaporization. In addition, Figure 6b shows a thin rope that appears "raft"-like, unlike the cylindrical shape of unsupported SWNTs observed in TEM images. We have observed this conformation on the Au substrate in several small ropes,[27] where it appears that the energy of a thin rope on a supported surface is minimized by increased nanotube−substrate contact area.[28]

Chemically Etched SWNT Ends. Much effort has been directed toward chemical modification of carbon nanotube ends, from tethering Au particles through thiol-linker molecules to organic reactions at the ends of carbon nanotube probe microscopy tips.[24,29] Investigations of the structure of the ends of the etched samples described above by STM provide a unique opportunity to help elucidate the consequences of etching reactions. The insets of Figures 7a and 7c show large-scale STM images of two etched nanotubes with different chiral angles, −23° and −16°, respectively. Closer inspection reveals that, unlike capped ends, the etched ends appear tapered with respect to the middle of the nanotube and cut at an angle. Indeed, analysis of high-resolution images shows that (1) different helicity tubes have different taper angles and (2) the cut ends are parallel to the *chair*-edge direction (whose lattice sites are separated by 0.426 nm). These results suggest that there is an energetic preference to produce ends along the armchair direction, and that it should be possible to predict the structure of etched ends. Consistent with our finding of *chair* edges, calculations have predicted that an exposed armchair edge is 0.8 eV/ atom more stable than a zigzag edge.[30]

To predict the structure of an etched SWNT end, consider Figure 8. As a result of etching, an unrolled (n,m) nanotube edge may be exposed along two different armchair directions **A** or **B** (Figure 8a). Our high-resolution STM images (Figures 7b and 7d), which show sharply cut ends, suggest that the *chair*-cut direction along **A** (i.e., 60° cut) is preferred over **B**. Models of this roll-up process as well as different spatial perspectives are shown in Figure 8b. This model proposes several geometric characteristics that have been verified using atomically resolved nanotube STM images. First, in our model the etched length L (in Figure 8b) of a tube is solely defined by the tube diameter D and angle ϕ:

$$L/D = \pi/(\tan(30 - \phi) + \tan(30 + \phi)) \qquad (3)$$

Second, the cut ends are parallel to the armchair directions given by the (n,m) indices of the tube. From the experimental images, L is determined from the approximate position on the tube where the tube diameter begins to thin. Indeed, the experimentally measured $L/D = 2.6$ and 2.3 for Figures 7a and 7c respectively, are in reasonable agreement with calculated $L/D = 2.7$ and 2.5 from eq 3 above. In addition, ball-and-stick models of the nanotube ends etched along **A** reproduce the edge shape and direction of the experimental images (Figures 7b and 7d). We believe that this simple model, which accounts for most of the experimental observations, will have important implications to several areas including (1) chemical functionalization of carbon nanotube ends and (2) the creation of ultrahigh-resolution probe microscopy tips.

One-Dimensional Band Structure of SWNTs

The characterization of semiconducting and metallic SWNTs with subtle changes in structure confirms the remarkable electronic behavior of the nanotubes and represents a significant step forward in understanding these 1D materials. In addition, the ability to probe simultaneously atomic structure and electronic properties provides a unique opportunity to investigate further several interesting properties of these 1D materials. These properties include, for example, the detailed density of states (DOS) of the nanotubes, the role of symmetry breaking distortions on the electronic character of nanotubes, and the electronic properties of defect and end electronic states. We address these interesting issues below and compare quantitatively our experimental results with theory. We start our discussion with an introduction to the 1D band structure and calculation of the DOS of SWNTs.

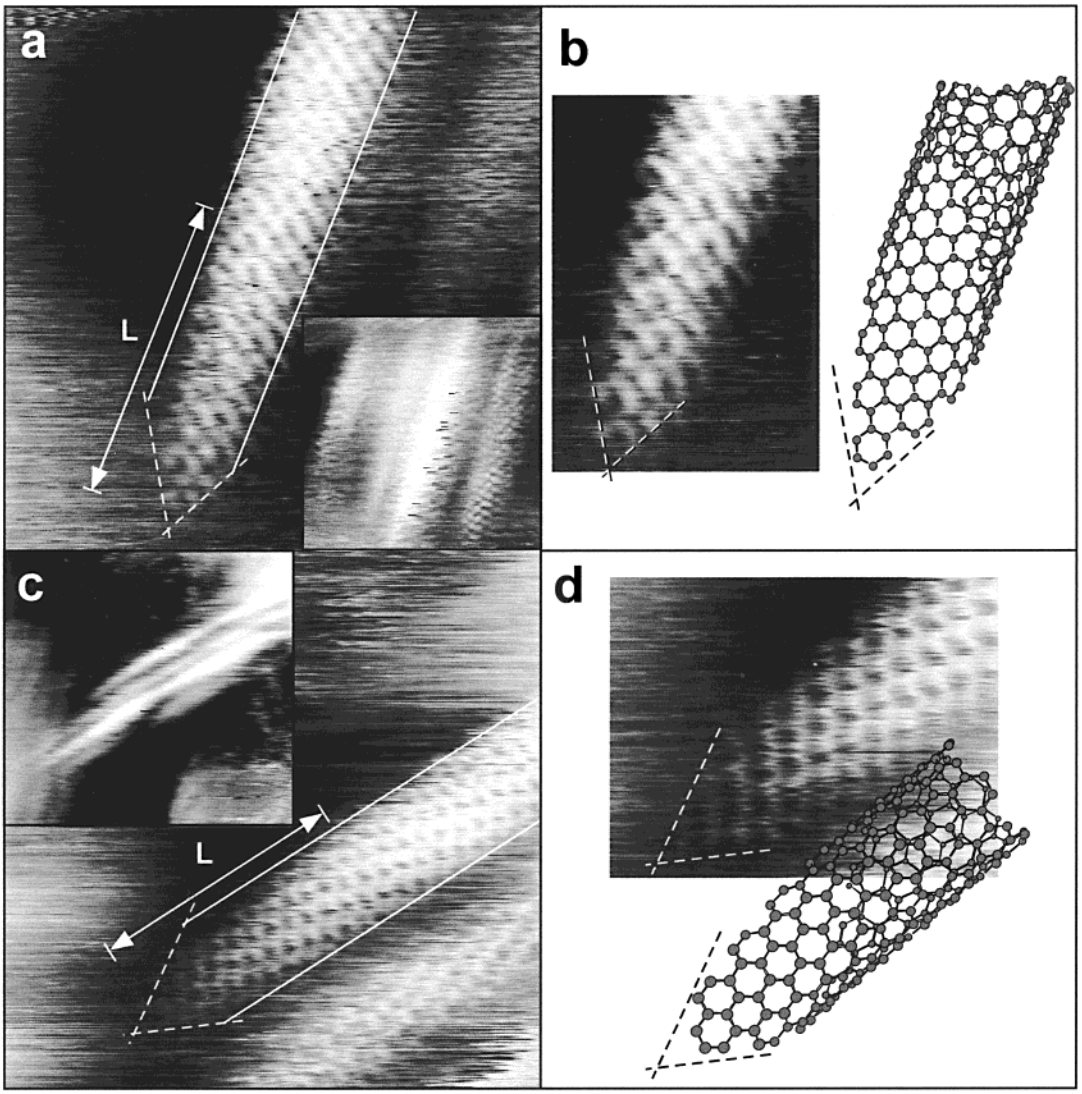

Figure 7. (a) STM image of an etched SWNT end. Dashed lines indicate the 60° cut along the *chair* direction. The etched length L is indicated by the distance between the white arrows. The chiral angle of this nanotube is −16°. (inset) Large-scale STM image indicating the size and shape of the chemically etched rope. (b) STM image of the etched end in (a) with its ball-and-stick representation simulated from our proposed model. The dashed lines indicate the 60° cut. (c) STM image of an etched SWNT end. Dashed lines indicate the 60° cut along the *chair* direction. The etched length L is indicated by the distance between the white arrows. The chiral angle of the tube is −23°. (inset) Large-scale STM image showing the end of a small rope. (d) STM image of the etched end in (c) with its ball-and-stick representation generated from our proposed model. The dashed lines indicate the 60° cut.

Tight-Binding Band Theory. Signature features in the DOS of a material appear at the band edges and are commonly referred to as van Hove singularities (VHS). A general expression for the density of states D(E) in d-dimensions is[31]

$$D(E) = \left(\frac{L}{2\pi}\right)^d \int \frac{\mathrm{d}k^d \delta(k(E) - k)}{|\nabla_k(E)|} \qquad (4)$$

where E is the energy, L is the dimension size, k is the wavevector, and ∇_k is the gradient with respect to k. At a band edge, the denominator $|\nabla_k(E)| \rightarrow 0$, and singularities arise in the DOS at E. These singularities, VHS, are characteristic of the dimension of a system. In three dimensions, VHS are kinks due to the increased degeneracy of the available phase space, while in two dimensions the VHS appear as stepwise discontinuities with increasing energy (Figure 9a). Unique to one-dimensional systems, the VHS are manifest as peaks. Hence, SWNTs and other 1D materials are expected to exhibit spikes in the DOS due to the 1D nature of their band structure.

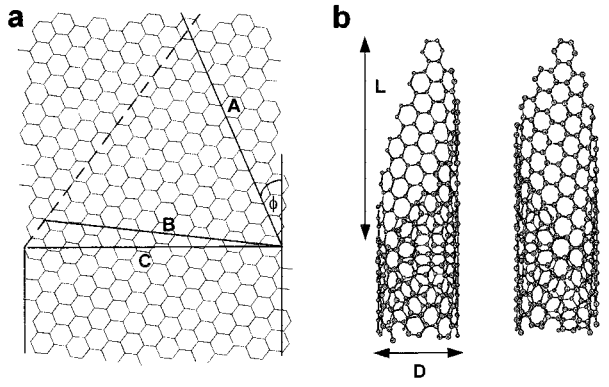

Figure 8. (a) Graphene strip for a (9,6) SWNT. **A** and **B** indicate possible stabilized *chair* directions after etching, with **A** at 60° and **B** at 120°. **C** is the roll-up vector and perpendicular to the tube axis, which is indicated by the vertical lines. The angle ϕ is defined on the SWNT. (b) Front and back perspective views of an etched (9,6) nanotube with the etched length L and diameter D as indicated in the figure.

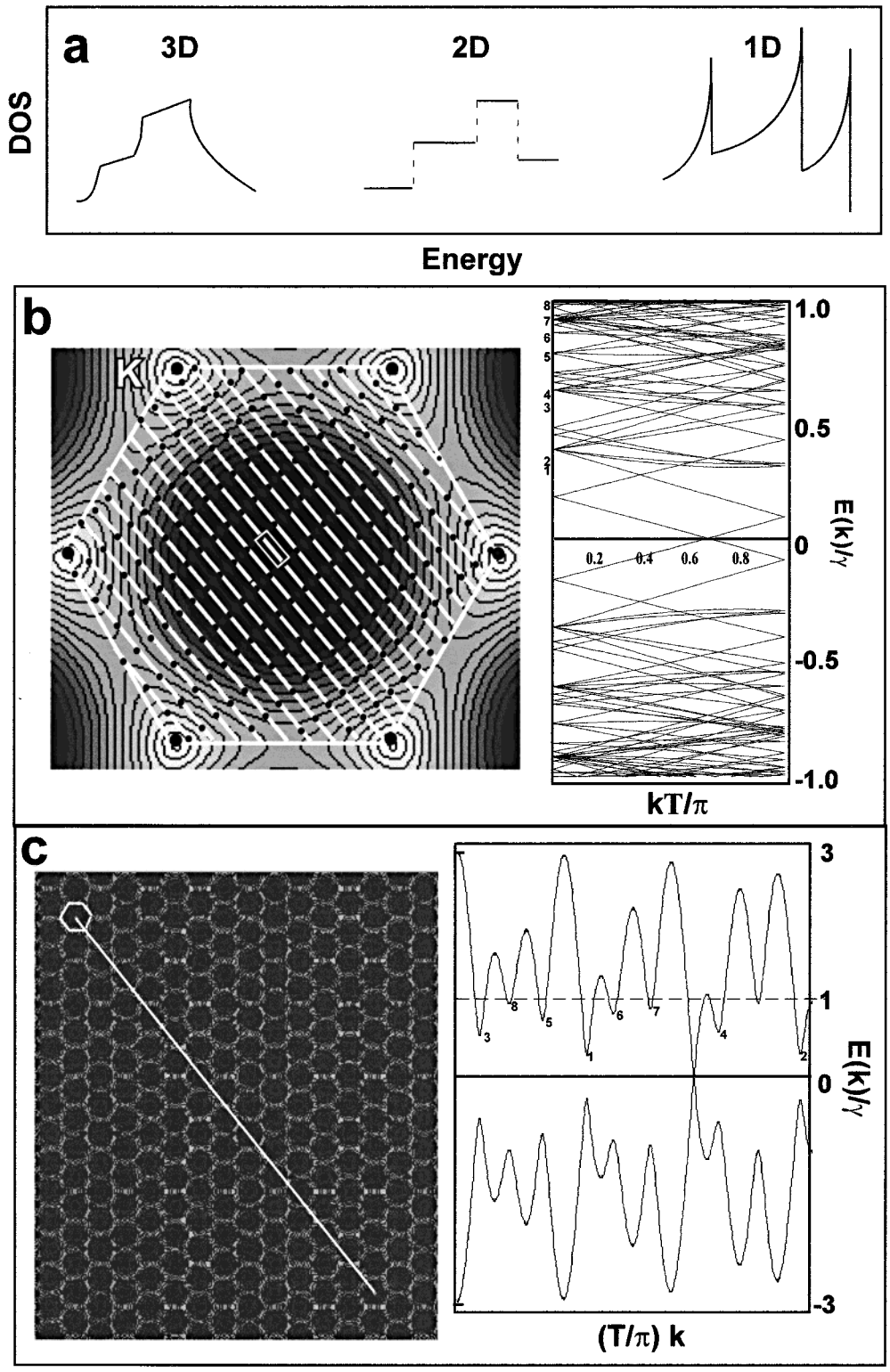

Figure 9. (a) Schematic of features in the density of states for 3D, 2D and 1D. (b) Zone-folded representation of the 1D subbands for a (13,7) SWNT. The distance between the black dots segmenting these parallel white lines represents the size of the tube's Brilluoin zone, with the first zone indicated by the white rectangular box. The black dots at the corners of graphene's hexagonal Brilluoin zone are the graphene **K** points. (right) The energy dispersion for a (13,7) nanotube described in the zone-folding representation. (c) Extended zone representation of the zone-folded subbands into a single line. (right) The resulting energy dispersion described in this is a single band. The same VHS in the zone-folding and extended zone schemes (up to $1\gamma_o$) are illustrated by their corresponding numbers.

One simple way to derive the tight-binding band structure of a SWNT is the zone-folding method.[1] As discussed previously, the allowed states for the (n,m) SWNT lie on a set of parallel lines that satisfy eq 1 in reciprocal space along the tube axis (white parallel lines in Figure 9b). Note that the unit cell length T may vary greatly for nanotubes of different structural symmetry, and it follows that a larger T results in a smaller BZ for the nanotube (since the zone boundaries are given by $\mathbf{k} = \pm\pi/T$). The first BZ of the (n,m) SWNT is the line segment of length $2\pi/T$ at the center of the first BZ of graphene, indicated by the white rectangular box in Figure 9b. To construct the energy band diagram, the 1D subbands are segmented into units

of $2\pi/T$ and then mapped into the first BZ of the SWNT by a linear combination of the nanotube's reciprocal lattice vectors. Assuming the values of the 2D energy dispersion relation of graphene along the segments, the 1D band structure is thus constructed and depicted to the right of Figure 9b for a (13,7) nanotube.

Since chiral SWNTs have unit cells that can be significantly larger than those of achiral SWNTs of similar diameter, the band structure of chiral SWNTs appears complicated compared with achiral ones due to a larger number of bands within a smaller BZ. It might be expected that these chiral nanotubes exhibit a larger number of VHS than achiral ones since, in typical materials, electronic bands open up gaps at the zone boundary (due to the crystal potential) and each band contributes a VHS at the zone boundary. However, in SWNTs, the complexity of the band structure originates from the fact that chiral SWNTs have large unit cells due to their low structural symmetry. This imposed complexity can be removed by working in the extended zone scheme of the graphene reciprocal lattice. As shown in Figure 9c, most of the 1D bands in the reduced zone scheme (Figure 9b) join together without $dE/dK \rightarrow 0$; thus, not every "band" in the zone-folded representation contributes a VHS. Indeed, as indicated up to $1\gamma_o$ in Figures 9b and 9c, the same number of VHS are produced in the extended zone scheme as in the reduced zone scheme.

We calculate the SWNT density of states from the zone-folded energy band diagram by summing the number of electrons at every level. The integral in eq 4 may be numerically evaluated with $d = 1$. First, the k-range is divided into a large number of k points, and the derivative dE/dk is calculated. Next the energy range is divided into a large number of bins, and dk/dE is summed for every E. The resulting DOS histogram is then broadened by a lorenztian of specified width.

However, even without an explicit calculation of the DOS for the 1D nanotube, a simple picture for understanding the relation of VHS to the diameter of a SWNT can be constructed by considering the subbands near **K**.[21] We illustrate this method with representative semiconducting and metallic nanotubes, (7,6) and (7,7), respectively. Figure 10a depicts the subbands of (7,6) indices around **K**, and the DOS for these indices is displayed on the right. The position of the 1D subbands is given by eq 1. To lowest order, the 2D energy dispersion of graphene is linear in **k** and radially symmetric around **K**. Hence the distance between the subbands that result in VHS to **K** is $|\mathbf{k} - \mathbf{k}_F|$.

For semiconducting SWNTs, the first band edge in the DOS arises from the subband nearest to **K** (indicated by ▼), a distance $\delta = |\mathbf{k}_▼ - \mathbf{k}_F| = 2\pi/3C_h$ away, the second band edge results from ▲ (2δ from **K**), and the third band edge arises from ■ (4δ from **K**). Thus, the VHS spacing characteristic of semiconducting nanotubes is $1-2-4$ from E_F. Figure 10b illustrates a similar concept for metallic tubes, except the subband nearest to **K** (3δ from **K**) gives rise to the first VHS. The subband that crosses **K** accounts for the nonzero DOS at E_F. Hence, the VHS spacing representative of metallic nanotubes is $1-2-3$ (with spacing $3\delta-6\delta-9\delta$) from E_F. One obvious but important observation is that the energy difference between the first set of VHS in the DOS for similar diameter nanotubes [e.g., (7,6) and (7,7)] is three times larger for metallic tubes than for semiconducting tubes. Analogous to $E_g = 2\gamma_o a_{C-C}/d$ for semiconductors, the gap between the first VHS for metallic tubes is $E_g^m = 6\gamma_o a_{C-C}/d$.[32]

Recent theoretical work suggests that semiconducting (or metallic) SWNTs of similar diameters will have similar VHS near the Fermi level in the DOS, independent of chiral angle.[21]

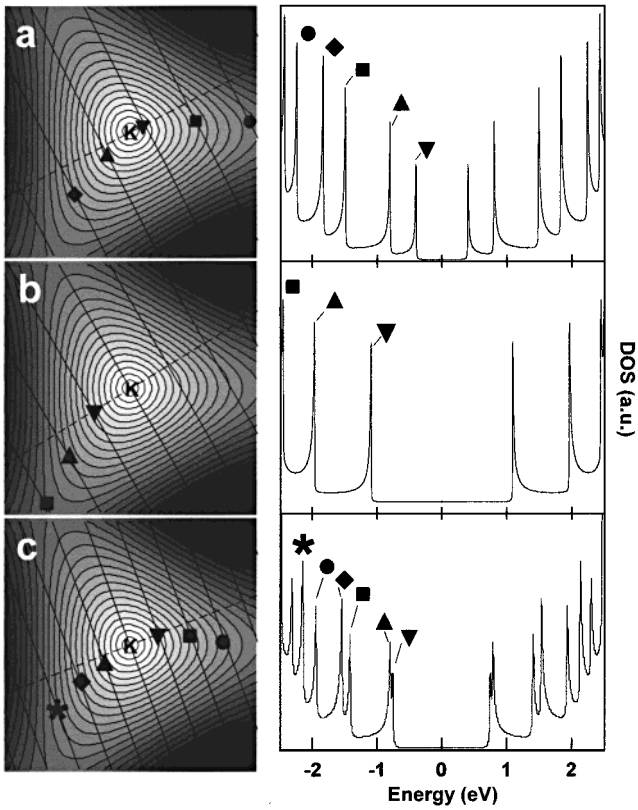

Figure 10. (a) Energy dispersion of the π band of a graphene sheet near **K**. The solid lines correspond to the (7,6) 1D bands obtained by zone-folding. Symbols are located at the positions where VHS occur in these 1D bands. The corresponding DOS from a π-only tight-binding calculation is shown on the right. (b) Same as (a) but for (7,7) bands. (c) Same as (a) but for (13,7) bands. The dashed line perpendicular to the 1D subbands guides the eye to where the positions of the VHS would occur if the energy dispersion around **K** were isotropic.

This is evident from the model we have described above. For instance, the VHS spacing for semiconducting tubes is $1\delta-2\delta-4\delta$ where $\delta = 2\pi/3C_h = 2/3d$. This spacing depends only on the diameter and not the helicity of the nanotube. Although different helicities result in different approach angles of the parallel subbands to **K**, the subband spacing, 3δ, is only diameter dependent; hence, independent of chiral angle, similar diameter nanotubes will have a similar number of VHS near E_F.

In the above discussion, we have assumed that the energy dispersion is isotropic around **K**; however, the energy dispersion becomes anisotropic away from **K**. Effects of this anisotropy are evident in Figure 10c, where for these (13,7) indices, the first two VHS in the 1D bands closest to **K** (depicted by ▼,▲) have a smaller splitting in energy than the next two VHS (depicted by ■,◆) due to the decreasing anisotropy near **K**. In addition, the integer VHS spacing derived above should be treated only as a schematic tool to describe the major differences in the DOS of semiconducting and metallic tubes. Since the energy dispersion is no longer linear at larger energies away from **K**, the energy position of the subband that contributes to the VHS will deviate slightly. This can be seen clearly in Figures 10a−c, where the symbols do not lie directly on the dotted line. Finally, this description is most valid for larger diameter semiconducting tubes since the subbands that give rise to VHS are closer to k_F than the subbands for metallic nanotubes.

STM Experiments. We have measured the electronic band structure experimentally by making tunneling spectroscopy measurements over an extended energy range.[33] When spectroscopic measurements are made on atomically resolved

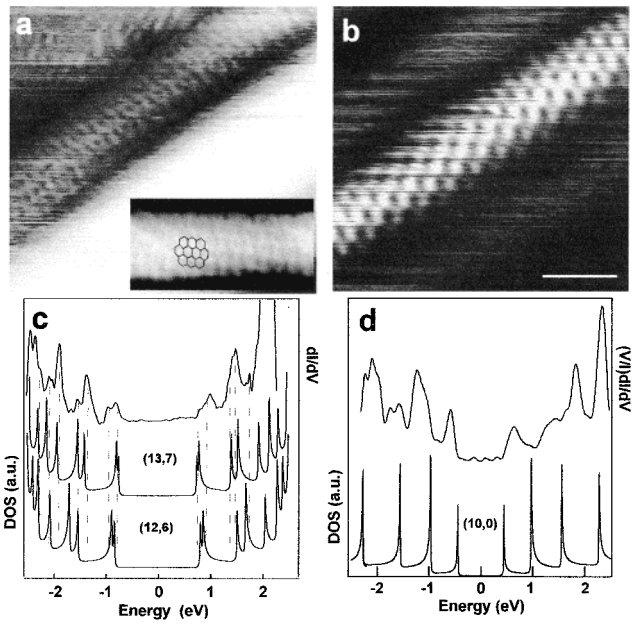

Figure 11. (a) STM image of SWNTs recorded with $I = 0.12$ nA and $V = 0.55$ V. Tunneling spectra were recorded on the isolated upper tube. The scale bar is 1 nm. The inset shows an atomic resolution image of this tube. A portion of a hexagonal lattice is overlaid to guide the eye. (b) STM image of a SWNT on the surface of a rope recorded with $I = 0.12$ nA and $V = 0.60$ V. The scale bar is 1 nm. (c) Comparison of the DOS obtained from experiment (upper curve) and a π-only tight-binding calculation for the (13,7) SWNT (second curve from top). The broken vertical lines indicate the positions of VHS in the tunneling spectra after consideration of thermal broadening convolution. The calculated DOS for a (12,6) tube is included for comparison. Adapted from ref 33. (d) Comparison of the DOS obtained from experiment (upper curve) and calculation for the (10,0) SWNT (lower curve).

nanotubes, it is also possible to compare the experimental DOS quantitatively with the tight-binding theory described above. An atomically resolved STM image of several SWNTs is shown in Figure 11a. The upper isolated tube that rests on the Au surface has indices (13,7). Current vs voltage measurements exhibit a linear response at $V = 0$ as expected for a metal (not shown)[33] and shows steps at larger voltages that correspond to a series of sharp peaks in the dI/dV. These peaks correspond to the VHS resulting from the extremal points in the 1D energy bands.

We have made a direct comparison of these experimental data to the theoretical electronic band structure calculated using the π-only tight-binding model described above. Significantly, our spectroscopy data show good agreement with the calculated DOS for the (13,7) tube (Figure 11c). The agreement between the VHS positions determined from our calculations and dI/dV data are especially good below E_F, where the first seven peaks correspond well. The peak splitting due to the anisotropy around **K** is also reproduced in the dI/dV. We also note that the gap, E_g^m, between the first VHS in this metallic tube is in agreement with the simple prediction discussed earlier; that is, $E_g^m = 6\gamma_o a_{C-C}/d = 1.6$, where γ_o is the value determined from semiconducting tubes. Above the Fermi energy some deviation between the experimental data and calculations exists. The observed differences may be due to band repulsion, which arises from curvature-induced hybridization.[34] We have also investigated the sensitivity of the VHS to variations in the (n,m) indices by calculating the DOS of the next closest metallic SWNT; that is, a (12,6) tube. It is worth noting that the poor agreement in this case demonstrates that subtle variations in diameter and helicity do produce experimentally distinguishable changes in the DOS.

In addition, we have characterized spectroscopically a small-diameter semiconducting nanotube (Figure 11b), whose indices we assign as (10,0). Similar to the above metallic (13,7) nanotube, the normalized conductance exhibits relatively good agreement with the calculated (10,0) DOS below E_F but poorer agreement above (Figure 11d). However, the π-only DOS calculation does not include π/σ and π^*/σ^* mixing due to curvature. This hybridization of π/σ orbitals is believed to produce more pronounced effects on the conduction band,[34] and this might explain the observed deviations. Additional work is needed to resolve this point. These results show clearly that the VHS spikes in the electronic band structure, which are characteristic of 1D systems, can be measured experimentally and agree well with the DOS calculated using π-only tight-binding models.

Symmetry Breaking Interactions. The above analyses neglect perturbations to the electronic structure of SWNTs due to interactions with the substrate and other nanotubes. The good agreement between spectroscopy data obtained on isolated nanotubes and calculations suggest that the substrate does not perturb strongly the band structure. We expected that nanotube−nanotube interactions within a tightly packed rope could, however, modify the electronic properties.

To examine this point we recorded atomically resolved images and spectroscopy data on nanotube ropes. Figure 12a shows an example of an armchair (7,7) tube buried within a bundle. The armchair nanotubes are particularly important because the band crossing at E_F makes them rigorously metallic. Spectroscopy data recorded on the (7,7) tube shows that the first VHS and electronic density prior to the VHS agree well with calculation. However, these measurements also show reproducibly a small, ~0.1 eV, gap at E_F that is not observed on the surrounding substrate.

The appearance of this gap is surprising in the armchair tubes, and we believe this feature arises from interactions with other tubes in the rope. Qualitatively, the gap can be understood in terms of mixing of the π and π^* bands that is allowed by the broken symmetry of the rope environment. In an isolated (n,n) armchair tube, the n-fold mirror planes along the axis prevent mixing of symmetric (π) and antisymmetric (π^*) states. When this rotational symmetry is broken, mixing occurs and a gap (an avoided crossing) occurs (Figure 12c). Notably, detailed calculations on a (10,10) rope containing a lattice of (10,10) tubes show that the broken symmetry of a rope can indeed open a pseudogap in the DOS of armchair SWNTs.[35] We also note that small gaps have been predicted for (n,0) metallic nanotubes due to curvature-induced mixing of s and p orbitals.[7,14] These gaps have not been observed in experiments to date[11] and represent an important area for future investigation.

Localized Structures in SWNTs

So far we have discussed the electronic properties of defect-free SWNTs. However, defects are occasionally observed in these seemingly infinite carbon cylinders. The electronic properties of localized SWNT structures, such as bends and ends,[36−38] are essential to proposed device applications. Below we describe selected examples of structures that have been characterized with atomically resolved imaging and spectroscopy.

Bent Nanotubes. Kinks and bends in carbon nanotubes can arise either from the insertion of a pentagon−heptagon (5−7) pair in the hexagonal network or from mechanical distortions

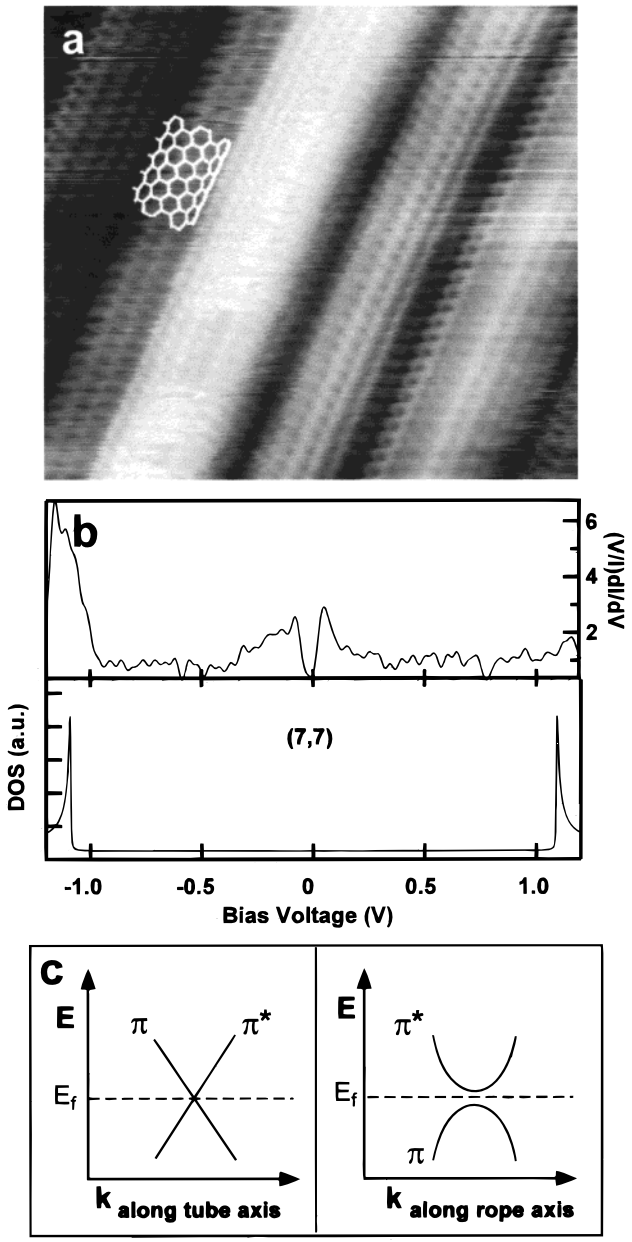

Figure 12. (a) STM image of a SWNT rope recorded with $I = 0.12$ nA and $V = 0.45$ V. The SWNTs within the rope exhibit armchair-like atomic structure. A 2D projection of the lattice for a (7,7) armchair is shown. (b) $(V/I)dI/dV$ recorded on the (7,7) tube is shown and compared with the calculated DOS for a (7,7) tube. Four similar curves were recorded at points along the tube, although only one data set is shown for clarity. The calculated van Hove singularities are found to agree relatively well with the experimental data except for the small gap at 0 V. This gap is attributed to broken rotational symmetry in the armchair tube. (c) (left) Schematic of crossing linear π and π^* bands in an isolated armchair nanotube. (right) Schematic of an avoided crossing of the bands in an armchair nanotube rope which causes a pseudogap in the DOS.

and bending. A variety of structures with (5−7) defects have been investigated theoretically,[36,37,40,41] although these have yet to be characterized experimentally by atomically resolved STM and tunneling spectroscopy. In addition, structural deformations can occur if a nanotube conforms to topological features[42] (e.g., steps) on the substrate and/or when spin-coating a nanotube solution onto the substrate surface.

An atomically resolved SWNT bundle that contains a sharp kink is shown in Figure 13. The bend angle defined by this kink is approximately 60°. For the purposes of this example,

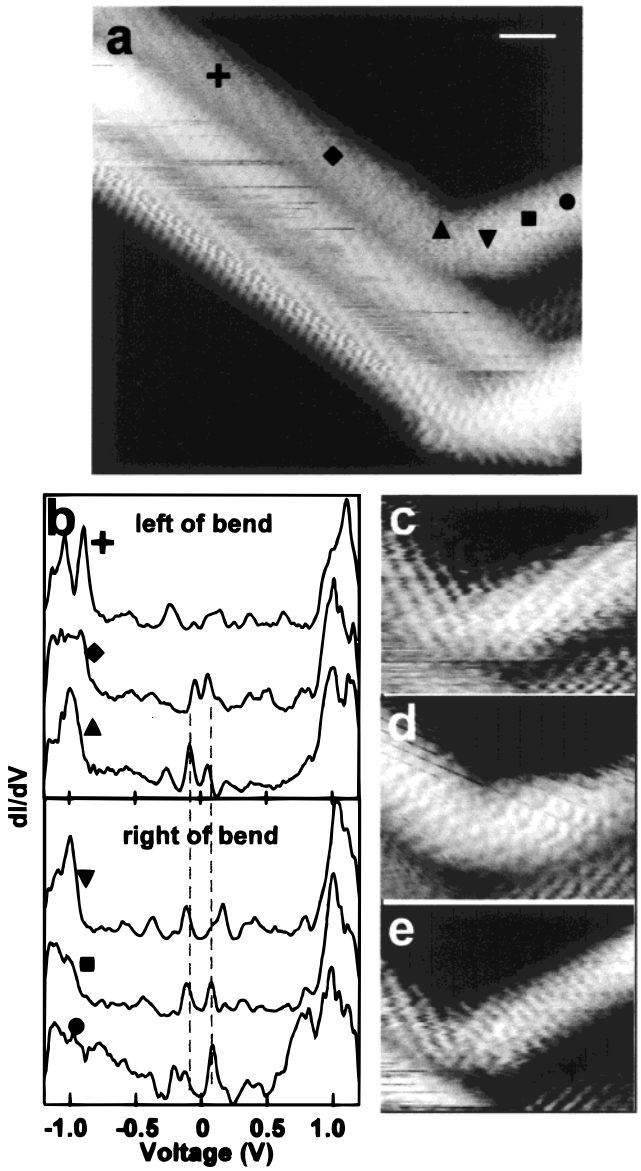

Figure 13. (a) STM image of a ∼60° bend in a rope of SWNTs recorded at $I = 0.12$ nA and $V = 0.55$ V. The symbols correspond to locations where I−V were measured. The scale bar is 1 nm. (b) Differential conductance calculated from the locations indicated in (a). The upper portion of the graph is spectroscopy performed on the left side of the bend over 5 nm. The lower portion of the graph is spectroscopy performed on the right side of the bend over 2 nm. The dashed lines highlight the low energy features. (c−e) STM images recorded at bias voltages of −0.15, 0.15, and 0.45 V, respectively.

we focus on the upper tube in the bundle. It is difficult to unambiguously assign the origin of the bend to 5−7 defects or mechanical strain. We expect that the 5−7 defects necessary to produce such a large angle, if present, would be located on the upper and lower sides of the nanotube, and thus be difficult to view directly by STM. Despite our inability to image the sides, we believe that evidence suggests the tube was bent by mechanical forces. First, the entire SWNT bundle is bent at the same angle and it is improbable that tubes with different helicities would have the distinct 5−7 defect structures needed to produce the same bend angles. Second, we find that the chiral angle on both sides of the bend in the upper tube is the same within experimental error. Since 5−7 defects typically produce a change in chirality, this observation suggests the bend has a different (i.e., mechanical) origin.

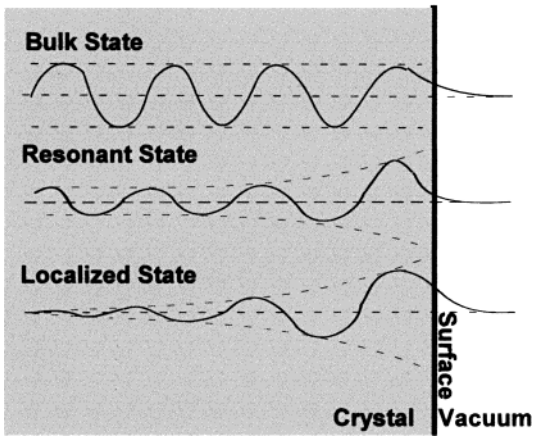

Figure 14. Schematic of three different types of surface states and their amplitude within a bulk crystal.

Tunneling spectroscopy was used to characterize the electronic properties of the bent tube. The I−V measurements were performed at the positions indicated by the symbols in Figure 13a, and their corresponding d*I*/d*V* are displayed in Figure 13b. The position of the van Hove peaks and I−V curves (not shown) indicate that the tube is metallic. Significantly, the data also show new features at low bias voltages on either side of the bend. These peaks are likely due to the presence of the bend, since five nanometers away (+) from the kink, the sharpness and prominence of these features have greatly diminished. Notably, recent calculations on bends in armchair tubes show similar low energy features in the DOS for similar bend angles.[39] One application of a bend and the resulting low energy peaks would be to serve as sites of enhanced chemical reactivity. Alternatively, reversible bending could serve as the basis for electronic devices with modulated conduction.

Last, the bend region was further investigated using bias-dependent STM imaging. On the right side of the bend, a superstructure on the tube is observed at the biases of the localized peaks (Figures 13c and 13d). Figure 13c shows stripes parallel to the zigzag direction of the tube and Figure 13d displays a triangular ring structure, where the spacing between nearest-neighbor rings is ca. 0.42 nm (the zigzag spacing). These new electronic features could be due to electron scattering and interference at the defect site.[43] Although the bias voltage, 0.45 V, at which Figure 13e was imaged is not at a prominent peak in the d*I*/d*V*, some electronic structure can be seen extending ∼1.5 nm to the right of the bend. However, this additional structure diminishes and an unperturbed atomic lattice is observed, consistent with the spectroscopic measurements. Further experimental and computational work is needed to elucidate clearly these interesting observations.

End Structure of SWNTs. Another example of localized geometric structures in nanotubes are the ends. Analogous to the surface states of a 3D crystal and the edge state of a 2D electron gas, end states are expected at the end of the 1D electron system. The ends of a 1D electronic system can be considered as the "surface" of the 1D bulk. Figure 14 shows a schematic of the wave function for a bulk state and two different types of surface states. Bulk states exhibit constant amplitudes far away from the surface, and these states diminish exponentially in amplitude as they approach the surface. Due to the sudden change of the crystal potential energy at the crystal−vacuum boundary, two general types of end states, which exhibit localized features at the interface, are possible.[44] If the energy of this end state falls into the forbidden energy gap of the bulk, the surface state is localized and the wave function has maximum amplitude at the surface (third curve, Figure 14). Alternatively, the energy of a surface state can be located inside the bulk band. In this case, the localized surface state can be connected to an extended bulk state and exhibit resonance behavior; that is, the wave function exhibits large amplitude at the surface but maintains finite amplitude in the bulk. Both resonant and localized states are possible at the ends of nanotubes. Resonant end states are expected for metallic nanotubes because there are no gaps in the 1D band structure of metallic SWNTs to localize the end states. In the same way, localized end states are possible for semiconducting nanotubes since they exhibit energy gaps in their DOS. In our STM experiments, we have been able to observe distinct types of electronic behavior at SWNT ends.[33]

The end states associated with carbon nanotubes may arise from pentagons in a capped end or an open nanotube.[45,46] In accordance with Euler's rule, a capped end should contain six pentagons. The presence of these topological defects can cause dramatic changes in the LDOS near the end of the nanotube. We have investigated carefully the electronic character of the capped nanotube end in Figure 15a. The rounded structure suggests strongly that the end is closed, although the atomic structure cannot be obtained since the tube axis is parallel to the image plane. Atomically resolved images enable us to assign the nanotube as (13,−2). The expected metallic behavior of the (13,−2) tube was confirmed in (*V*/*I*)d*I*/d*V* data recorded away from the end (Figure 15c). Significantly, spectroscopic data recorded at and close to the SWNT end show two distinct peaks at 250 and 500 mV that decay and eventually disappear in the bulk DOS recorded far from the tube end.

To investigate the origin of these new spectroscopic features, we carried out tight-binding calculations for a (13,−2) model tube terminated with different end caps (Figure 15b). The cap configurations are determined by the topological arrangement of the six pentagons.[47] Since cap structures with two or more adjacent pentagons create high curvature at the cap region and are not energetically favorable, these are not included in the number of possible cap structures, which is known as the independent pentagon rule (IPR).[1] However, we have included calculations on these models to test the validity of the IPR for the SWNT end. All of the models exhibit a bulk DOS far from the end (lower curve in Figure 15d); however, near the nanotube ends the LDOS show pronounced differences from the bulk DOS. The LDOS of model caps I and II shows well-defined peaks near E_F, which is much different from model cap III (which violates IPR). More importantly, the LDOS obtained from the calculation for caps I and II shows excellent agreement with the measured LDOS at the tube end, while cap III does not (Figure 15d). The positions of the two end LDOS peaks as well as the first band edge of cap I match well with those from the experimental spectra. These results suggest that the arrangement of pentagons is responsible for the observed DOS peaks at the SWNT ends, and that these pentagons are isolated from each other, in support of the IPR for SWNTs.

The nature of the DOS peaks at the nanotube end (are they resonant or localized states) was further investigated using bias-dependent STM imaging. At the bias of the strong DOS peak, −500 mV, the tip-nanotube separation $h(x)$ decays with increasing x, where x is the distance from the tube end (Figure 16a). The wave function probability normal to the tube axis, $|\Psi(x)|^2$, can also be expressed as an exponential decay,

$$|\Psi(x)|^2 = \int_0^{eV} \mathrm{LDOS}(x,E)\mathrm{d}E \propto \exp[k_d h(x)] \qquad (5)$$

where k_d is the decay constant. The value $k_d = 2.0$ Å^{-1} was

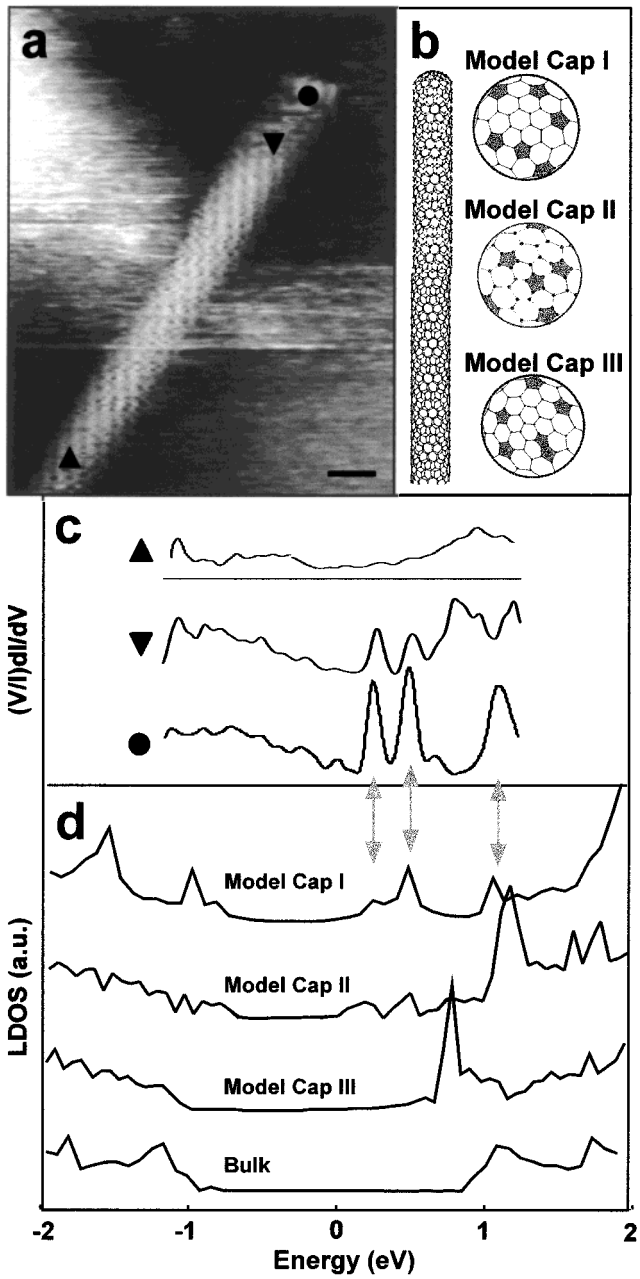

Figure 15. (a) STM image of the end of a SWNT recorded with $I = 0.15$ nA and $V = 0.75$ V. The scale bar is 1 nm, and the symbols correspond to the locations where the tunneling spectra in (c) were recorded. (b) A model (13,−2) SWNT with three different cap structures; the pentagons in the caps are shaded gray. (c) Experimental tunneling spectra from the end ●, near the end ▼, and far from the end ▲. (d) LDOS obtained from tight-binding calculations on capped (13,−2) tubes for caps I, II, and III, respectively. Similar features in ● and cap I are highlighted by gray arrows. The bulk DOS for all of the cap models are identical and is shown in the lowest curve. Adapted from ref 33.

obtained from the exponential decay in experimental current versus distance measurements. Hence, we can compare directly experiment with our calculation. This comparison shows that the calculated LDOS (0 to 500 meV) agrees well with experiment (Figure 16a) and, moreover, gives a decay length for the end state of ca. 1.2 nm. Our tight-binding calculation further suggests that this decay can be attributed to resonant end states.[33] Wave functions whose eigenenergies correspond to the LDOS peaks (250 meV, 500 meV) decay exponentially from the end into the bulk but retain a finite amplitude (Figure 16b). In addition, we find that wave functions with eigenenergies

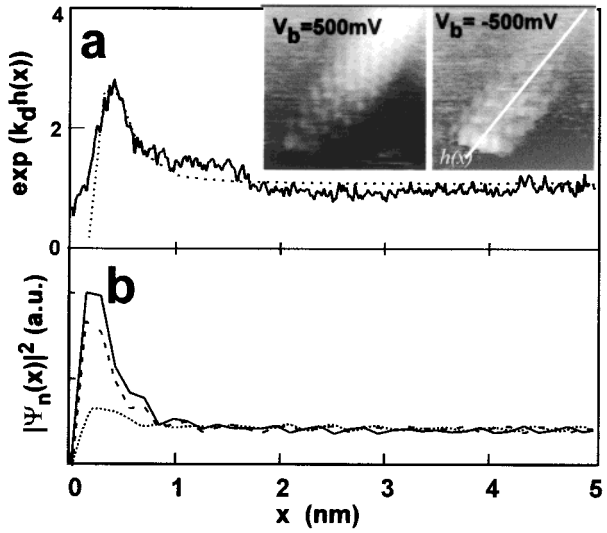

Figure 16. (a) (insets) STM images recorded at different voltages on the SWNT end in Figure 15. The white line indicates the $h(x)$ cross section. The solid line in (a) corresponds to $\exp[k_d\, h(x)]$, where $k_d = 2^{\cdot -1}$, and the dotted line is the integrated LDOS (0−500 meV) from our calculation. (b) The solid, broken, and dotted lines depict the wave function probability (arbitrary units), $|\Psi_n(x)|^2$, of cap I as a function of position x for eigenenergies of 500, 250, and 320 meV, respectively. Adapted from ref 33.

removed from the end state peaks do not decay with position from the end, and likewise, images recorded with bias voltages far from these points show little variation in $h(x)$. Taken together, these experimental measurements and calculations suggest quite clearly that the observed features are resonant end states.

Finally, we have observed bulk-like states at the ends of the chemically etched nanotubes (Figure 17). As discussed earlier, these etched ends are proposed to have a carbon−carbon bond edge along the *chair* direction. Moreover, it is likely that the edges are terminated (no dangling bonds) with oxidized organic groups[29] since the etching was carried out in oxidizing acid solution. A typical atomically resolved etched SWNT (Figure 17a), which was spectroscopically characterized is shown as an example. Notably, the $(V/I)\mathrm{d}I/\mathrm{d}V$ at the tube end and in the bulk (Figure 17b) exhibits very similar behavior, but with a reduced amplitude compared to the data taken at the very end (solid curve). The similarity of the LDOS for the end and bulk of the etched SWNT (with no evidence for low-energy localized states at end) is consistent with chemical termination of the open ends to eliminate dangling bonds.

Finite Size Effects in SWNTs

To this point in the Feature Article we have focused on SWNTs that have always retained characteristic features of a periodic 1D system. In this last section of the article, we touch on the question of what happens when this 1D system is made increasingly smaller. Conceptually, as the length of a SWNT is reduced one ultimately will reach the limit of a fullerene molecular cluster, a 0D object. In this regard, studies of finite-size SWNTs offer a unique opportunity to probe the connection between and evolution of electronic structure in periodic molecular systems (Figure 18a). Investigations of finite-sized effects in SWNTs are also important to the future utilization of nanotubes in device applications. Transport experiments on metallic SWNTs have shown that μm long tubes behave as Coulomb islands in single electron transistors.[48,49] Since the coulomb charging energy $E_c \propto 1/L$, shorter nanotubes would allow the working temperature of such devices to increase. In

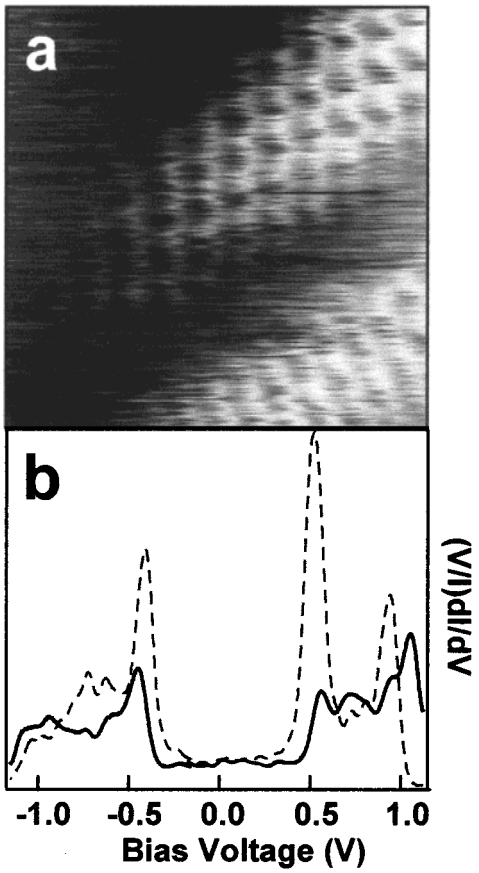

Figure 17. (a) STM image of the etched end shown in Figure 7c. (b) $(V/I)\mathrm{d}I/\mathrm{d}V$ measured at the end of the nanotube (solid curve) and 10 nm past the etched end (dashed curve). The tunneling spectra are almost identical and hence this end state is bulk-like.

addition, finite size effects should be visible at room temperature if $\Delta E > k_b T$; thus a resonant tunneling device may be conceived with nanotubes whose lengths are less than 50 nm. Since voltage pulses can be used to systematically cut nanotubes into these short lengths (Figures 18b and 18c),[50,51] STM/STS can in principle probe the transition from 1D delocalized states to molecular levels. In the following sections, we discuss our investigation of finite size effects in carbon nanotubes at length scales less than 10 nanometers.

An STM image of a nanotube shortened to six nanometers is shown in Figure 19a. Equally spaced tunneling current vs voltage measurements were performed along the nanotube's length, and the spectra were nearly identical at all positions along the tube. The averaged I−V curve shows a stepwise increase of current over a two-volt bias range (Figure 19d) which produces sharp peaks at low energies in the $(V/I)\mathrm{d}I/\mathrm{d}V$. Since the DOS of bulk metallic SWNTs is constant at low energies until the first band edges (ca. $\pm$ 1 eV), we can attribute these peaks to resonant tunneling through discrete energy levels resulting from the finite length of the SWNT. In addition, we have investigated the electronic properties of a slightly shorter nanotube (Figure 19b), roughly five nanometers long, with helicity opposite to the tube in Figure 19a. This nanotube also shows a stepwise increase of current in its tunneling spectra as well as slightly farther spaced peaks in its $(V/I)\mathrm{d}I/\mathrm{d}V$ (Figure 19e).

The observed peaks in the $(V/I)\mathrm{d}I/\mathrm{d}V$ may be attributed to electron confinement along the nanotube axis in finite-sized metallic tubes. The bulk metallic nanotube band structure is characterized by two linear bands (π and π^*) that cross the

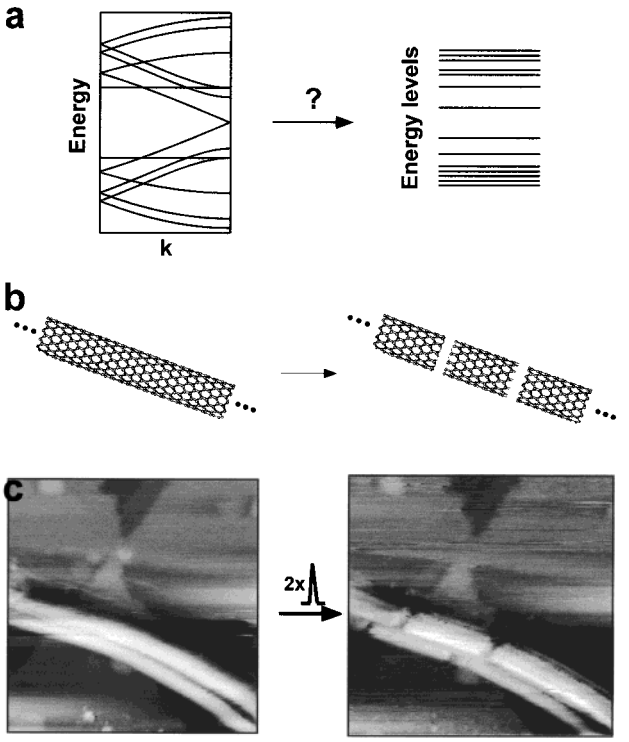

Figure 18. (a) Schematic diagram of the electronic transition from 1D to 0D: from a continuous band diagram to discrete energy levels. (b) Schematic of infinite nanotubes shortened into finite lengths by application of voltage pulses. (c) STM images depicting experimental realization of shortening nanotubes by voltage pulses.

Fermi energy, and these bands contribute a finite, constant DOS at low energies. Confinement of the electrons due to reduced axial lengths produces a discretization $\Delta k = \pi/L$ on the crossing bands, where L is the nanotube length. The intersection of Δk and the linear bands in the zone folding scheme results in an energy level spectrum. An alternative, simpler analysis of this problem is to consider the finite-length nanotube as a 1D particle-in-a-box, whose well-known eigenvalues (E) are $E = \hbar^2 k^2/2m$. The energy level spacing is easily derived:

$$\Delta E = \hbar^2 k_F \Delta k/m = h\upsilon_F/2L \approx 1.67 \text{ eV/L (nm)} \qquad (6)$$

where h is Planck's constant and $\upsilon_F = 8.1 \times 10^5$ m/s is the Fermi velocity for graphene.

To first order, analysis of the peak spacing for the finite-sized nanotubes (Figures 19a and 19b) agrees with this simple particle-in-a-box model. The former tube that is six nanometers long exhibits a mean peak spacing of approximately 0.27 eV. A six nanometer tube within this 1D box model would have an average level spacing $\Delta E \approx 1.67$ eV /6 = 0.28 eV. For the latter tube with its shorter length, the observed peak spacing is also wider, as expected from this model. Hence it appears that finite-sized metallic tubes exhibit behavior that is only length-dependent for similar diameter nanotubes. This observation is reasonable since the energy dispersion is isotropic near k_F and all the approach angles of the allowed 1D subbands have the same slope $\mathrm{d}E/\mathrm{d}k \propto \upsilon_F$. However, upon careful inspection of $(V/I)\mathrm{d}I/\mathrm{d}V$ for these two metallic nanotubes we observe small splittings of some peaks. The anisotropy around **K** becomes important and thus the two linear bands which cross the Fermi energy have different slopes.[52] If these bands now have marginally different slopes, the intersection of these bands with Δk, imposed by the finite length, will result in slightly different

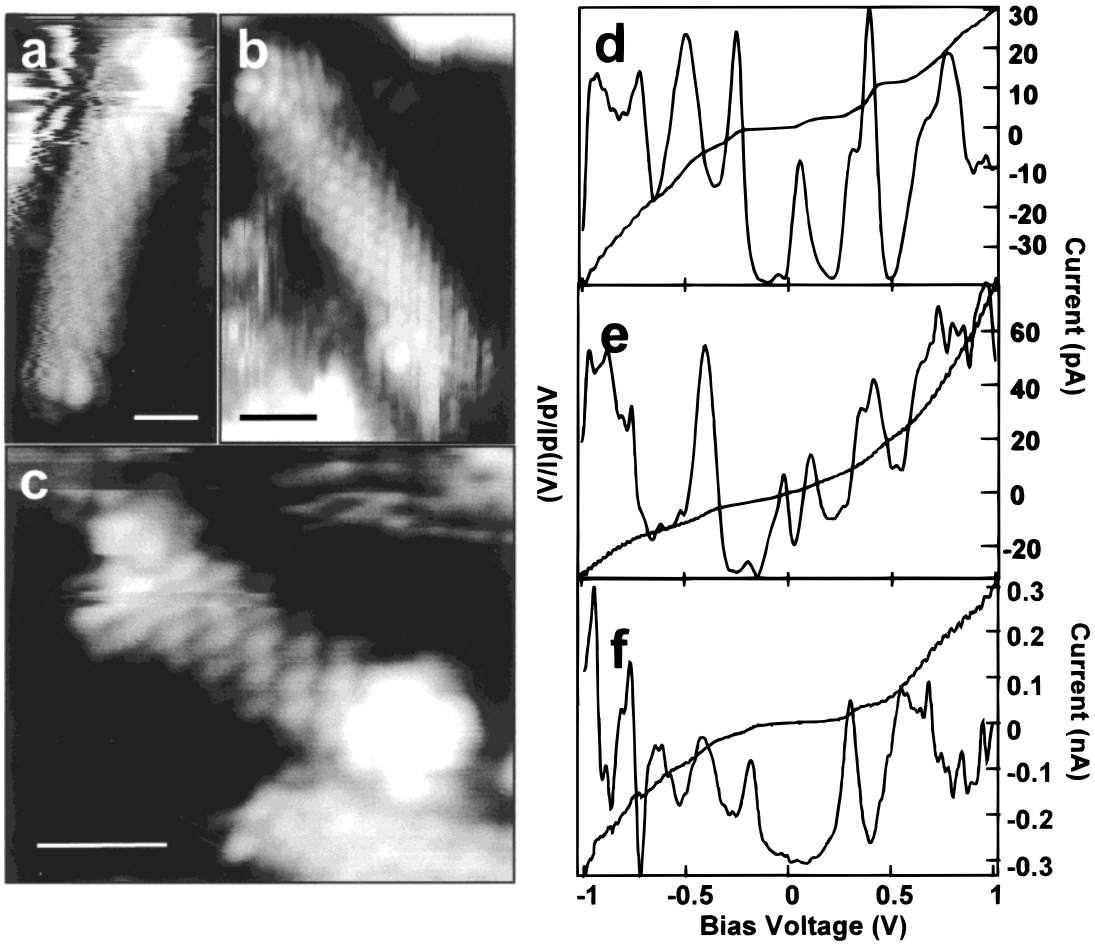

Figure 19. (a−c) STM images of SWNTs cut by voltage pulses and shortened into lengths of 6 nm, 5 nm, and 3 nm, respectively. (d−f) Averaged normalized conductance and I−V measurements performed on the nanotubes in (a−c), respectively. Six I−V curves were taken along the tube length and averaged together since the spectra were essentially indistinguishable.

$E(k)$ values, and this would account for the small splittings observed in the energy level spectrum.

In addition, we have interrogated further the transition from 1D bulk behavior to molecular behavior in studies of an atomically resolved nanotube three nanometers in length (Figure 19c). Similar to the aforementioned cut metallic nanotubes, tunneling spectra taken along its length do not show marked differences in the I−V measurements. The averaged $(V/I)\mathrm{d}I/\mathrm{d}V$ is shown in Figure 19e. The normalized conductance appears, however, quite different from the expected 1.67 eV /3 = 0.55 eV energy level spacing for a nanotube three nanometers long. We believe this reflects the limitations of this simple model and the need for a more detailed molecular model to explain adequately the electronic structure. Ab initio calculations of SWNT band structure have recently shown that the energy level spacing of finite-size tubes may be considerably different from that predicted from a Hückel model due to the asymmetry and shifting of the linear bands crossing at E_F.[52] In addition, several molecular computational studies have predicted that nanotubes less than four nanometers long should open a HOMO−LUMO gap around E_F, although its magnitude varies greatly among different calculation methods.[53,54] These studies have been performed on finite-sized, open-ended, achiral (n,0) zigzag and (n,n) armchair tubes. In quantum molecular calculations, symmetry considerations are important, and in this regard chiral nanotubes may exhibit drastically different electronic characteristics compared with achiral ones. Clearly, more sophisticated molecular and first principle calculations are required to fully understand nanotubes at such ultrashort length scales.

Coulomb Charging Effects in Nanotubes. In the experiments discussed above, the finite-sized nanotubes remained in good contact with the underlying substrate after cutting, and the voltage drop was primarily over the vacuum tunnel junction. If the nanotubes are weakly coupled to the surface, a second barrier for electron tunneling is created and these nanotubes may behave as coulomb islands and exhibit coulomb blockade and staircase features in their I−V.[55] The investigation of finite-sized nanotubes in the presence of charging effects is interesting since both effects scale inversely with length and thus can be probed experimentally. Below we describe one example of an atomically resolved nanotube quantum dot that has been characterized spectroscopically, and we compare the tunneling spectra with a modified semiclassical theory for coulomb blockade/single-electron tunneling.

An atomically resolved STM image of several SWNTs is shown in Figure 20a. The nanotubes rest perpendicular to a raft of nanotubes (after cutting) and are thus weakly coupled to the substrate. We concentrate our analysis on the nanotube indicated with an arrow whose length (L) and radius (R) are 7.5 and 0.5 nm, respectively. The tunneling current vs voltage exhibits a suppression of current at zero bias as well as relatively sharp, step-like increases at larger $|V|$ (Figure 20b), reminiscent of the coulomb blockade and staircase.[55] Noticeably in the tunneling spectra, the current step heights and widths are irregular. We attribute these irregularities in the conductance peak spacing and amplitude to contributions from the discrete level spacing of the finite-sized nanotube.[56]

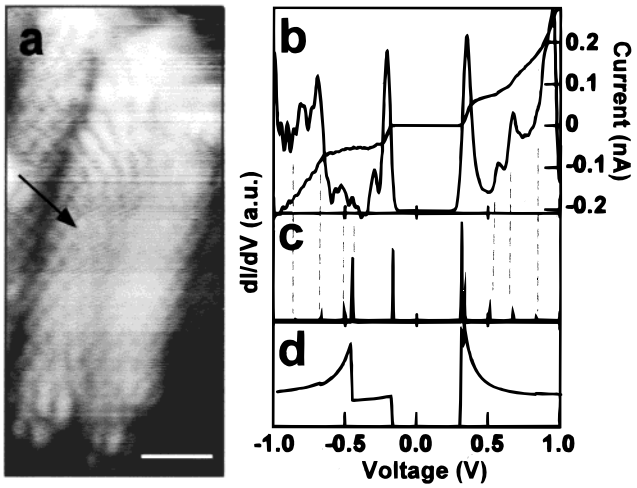

Figure 20. (a) STM image of SWNTs cut by voltage pulses recorded at $I = 0.12$ nA and $V = 0.75$ V. The scale bar is 1 nm. (b) Measured I−V and dI/dV performed on the tube in (a). Note the presence of zero current in the I−V denoting the presence of Coulomb blockade. (c) Numerical derivative of the I−V curve calculated by a semiclassical calculation. This calculation includes the level spacing of a 1D particle-in a box. The dashed lines highlight similar features in the derivative of the calculated I−V and the experimental dI/dV. (d) Same calculation as (c) except the nanotube DOS is treated as continuous. This is insufficient to describe the experimental data.

To interpret these complex tunneling spectra, we have modified a semiclassical double-junction model[57] to include the level spacing of the nanotube quantum dot. Our results from the previous section[51] enable us to estimate the average level spacing for this 7 nm tube to be $\Delta E \sim 1.67$ eV /7 = 0.24 eV. An initial starting parameter in this fitting procedure is an estimation of the nanotube−Au capacitance, C_1. The capacitance of a SWNT resting on a metal surface may be approximated by[58]

$$C = 2\pi\epsilon L/\ln\{[d+(d^2 - R^2)^{1/2}]/R\} \qquad (7)$$

where d is the distance from the center of the nanotube to the surface and ϵ is 8.85×10^{-3} aF/nm. Estimating $d \sim 1.9$ nm,[59] the geometric capacitance for the nanotube in Figure 20a is 0.21 aF. The calculated dI/dV that best fits the tunneling conductance is shown in Figure 20c and yields a Au−tube capacitance $C_1 = 0.21 \pm 0.01$ aF, in good agreement with the capacitance estimated by the geometry of the nanotube. In contrast, if the calculation neglected the level spacing of the nanotube dot, only the blockade region is reproduced well (Figure 20d). These studies demonstrate that it is possible also to study the interplay of finite size effects and charging effects in SWNT quantum dots of ultrashort lengths.

Conclusions

Scanning tunneling microscopy and spectroscopy have been used to characterize the atomic structure and tunneling density of states of individual SWNTs and SWNT ropes. We have shown that defect-free SWNTs exhibit semiconducting and metallic behavior that depends predictably on helicity and diameter. In addition, we have characterized the 1D VHS in the DOS for both metallic and semiconducting tubes and have compared our data with tight-binding calculations. The good agreement obtained between experiment and π-only calculations shows that much of the physics of SWNT band structure is captured with a "simple" π-only model, although deviations suggest that further work is necessary to understand fully how tube−tube interactions, which can produce broken symmetry, and curvature effects perturb the electronic structure of SWNTs. We have also observed and characterized spectroscopically localized structures in SWNTs such as bends and ends. These studies show the presence of sharp localized features that in many cases can be understood well using π-only models, although more subtle features, which may reflect electron scattering, will require more detailed experimental and theoretical focus to unravel. The characterization of electronic features at SWNT ends also has implications to understanding and developing the chemical reactivity of this material and to efficiently couple nanotubes for electron transport. Last, we have begun to probe the electronic properties of finite length scales. These studies show that it is possible to access readily a regime of "0D" behavior, where finite length produces quantization along the tube axis, and we believe opens up future opportunities to probe, for example, connections between extended and molecular systems. In short, we believe much of the fascinating overall structural and electronic properties of SWNTs are now in hand, but this really only has scratched the surface of these and other emerging 1D systems. Future work will be rewarded with answers to many fundamental scientific problems, and moreover, should push emerging concepts in nanotechnologies.

Acknowledgment. We thank C. L. Cheung for preparation of nanotubes and J. Liu and R. E. Smalley for chemically-etched samples. This work was supported by the NSF.

References and Notes

(1) Dresselhaus, M. S.; Dresselhaus, G.; Eklund, P. C. *Science of Fullerenes and Carbon Nanotubes*; Academic: San Diego, 1996.
(2) Yakobson, B. I.; Smalley, R. E. *Am. Sci*. **1997**, *85*, 324.
(3) Dekker, C. *Phys. Today* **1999**, *52*, 22.
(4) Treacy, M. M. J.; Ebbesen, T. W.; Gibson, J. M. *Nature* **1996**, *381*, 678.
(5) Wong, E. W.; Sheehan, P. E.; Lieber, C. M. *Science* **1997**, *277*, 1971.
(6) Yakobson, B. I.; Brabec, C. J.; Bernholc, J. *Phys. Rev. Lett*. **1996**, *76*, 2511.
(7) Hamada, N.; Sawada, S.; Oshiyama, A. *Phys. Rev. Lett*. **1992**, *68*, 1579.
(8) Mintmire, J. W.; Dunlap, B. I.; White, C. T. *Phys. Rev. Lett*. **1992**, *68*, 631.
(9) Saito, R.; Fujita, M.; Dresselhaus, G.; Dresselhaus, M. S. *Appl. Phys. Lett*. **1992**, *60*, 2204.
(10) Wildoer, J. W. G.; Venema, L. C.; Rinzler, A. G.; Smalley, R. E.; Dekker, C. *Nature* **1998**, *391*, 59.
(11) Odom, T. W.; Huang; J.-L.; Kim, P.; Lieber, C. M. *Nature* **1998**, *391*, 62.
(12) Lieber, C. M. *Solid State Comm*. **1998**, *107*, 607.
(13) Hu, J.; Odom, T. W.; Lieber, C. M. *Acc. Chem. Res*. **1999**, *32*, 435.
(14) Kane, C. L.; Mele, E. J. *Phys. Rev. Lett*. **1997**, *78*, 1932.
(15) Crespi, V. H.; Cohen, M. L.; Rubio, A. *Phys. Rev. Lett*. **1997**, *79*, 2093.
(16) Guo, T.; Nikolaev, P.; Thess, A.; Colbert, D. T.; Smalley, R. E. *Chem. Phys. Lett*. **1995**, *243*, 49.
(17) Thess, A.; Lee, R.; Nikolaev, P.; Dai, H.; Petit, P.; Rober, J.; Zu, C.; Lee, Y. H.; Kim, S. G.; Rinzler, A. G.; Colbert, D. T.; Scuseria, G. E.; Tomanek, D.; Fischer, J. E.; Smalley, R. E. *Science* **1996**, *273*, 483.
(18) Odom, T. W.; Huang, J.-L.; Kim, P.; Ouyang, M.; Lieber, C. M. *J. Mater. Res*. **1998**, *13*, 2380.
(19) Stroscio, J. A.; Feenstra, R. M. *Scanning Tunneling Microscopy*; Academic: New York, 1993.
(20) Everson, M. P.; Jaklevic, R. C.; Shen, W. *J. Vac. Sci. Technol. A* **1990**, *8*, 3662.
(21) White, C. T.; Mintmire, J. W. *Nature* **1998**, *394*, 29.
(22) White, C. T.; Robertson, D. H.; Mintmire, J. W. *Phys. Rev. B* **1993**, *47*, 5485.
(23) Rao, A. M.; Richter, E.; Bandow, S.; Chae, B.; Eklund, P. E.; Williams, K. A.; Fang, S.; Subbaswamy, K. R.; Menon, M.; Thess, A.; Smalley, R. E. *Science* **1997**, *275*, 187.
(24) Liu, J.; Rinzler, A. G.; Dai, H. J.; Hafner, J. H.; Bradley, R. K.; Boul, P. J.; Lu, A.; Iverson, T.; Shelimov, K.; Huffman, C. B.; Rodriguez-

Macias, F.; Shon, Y. S.; Lee, T. R.; Colbert, D. T.; Smalley, R. E. *Science* **1998**, *5367*, 1253.
(25) Hassanien, A.; Tokumoto, M.; Kumazawa, Y.; Kataura, H.; Maniwa, Y.; Suzuki, S.; Achiba, Y. *Appl. Phys. Lett*. **1998**, *73*, 3839.
(26) Falvo, M. R.; Taylor, R. M.; Helser, A.; Chi, V.; Brooks, F. P.; Washburn, S.; Superfine, R. *Nature* **1999**, *397*, 236.
(27) Wong, S. S.; Woolley, A. T.; Odom, T. W.; Huang, J.-L.; Kim, P.; Vezenov, D. V.; Lieber, C. M. *Appl. Phys. Lett*. **1998**, *73*, 3465.
(28) Hertel, T.; Martel, R.; Avouris, Ph. *J. Phys. Chem*. **1998**, *102*, 910.
(29) Wong S. S.; Joselevich, E.; Woolley, A. T.; Cheung, C. L.; Lieber, C. M. *Nature* **1998**, *394*, 52.
(30) Lee, Y. H.; Kim, S. G.; Tomanek, D. *Phys. Rev. Lett*. **1997**, *78*, 2393.
(31) Ashcroft, N. W.; Mermin, N. D. *Solid State Physics*; Holt, Rinerhart and Winston: New York, 1976.
(32) Rubio, A. *Appl. Phys. A. Mater*. **1999**, *68*, 275.
(33) Kim, P.; Odom, T. W.; Huang, J.-L.; Lieber, C. M. *Phys. Rev. Lett*. **1999**, *82*, 1225.
(34) Blasé, X.; Benedict, L. X.; Shirley, E. L.; Louie, S. G. *Phys. Rev. Lett*. **1994**, *72*, 1878.
(35) Delaney, P.; Choi, H. J.; Ihm, J.; Louie, S. G.; Cohen, M. L. *Nature* **1998**, *39*, 466.
(36) Lambin, P. H.; Lucas, A. A.; Charlier, J. C. *J. Phys. Chem. Solids* **1997**, *58*, 1833.
(37) Chico, L.; Crespi, V. H.; Benedict, L. X.; Louie, S. G.; Cohen, M. L. *Phys. Rev. Lett*. **1996**, *76*, 971.
(38) Han, J.; Anantram, M. P.; Jaffe, R. L.; Kong, J.; Dai, H. *Phys. Rev. B* **1998**, *57*, 14983.
(39) Rochefort, A.; Salahub, D. R.; Avouris, Ph. *Chem. Phys. Lett*. **1998**, *297*, 45.
(40) Meunier, V.; Henrard, L.; Lambin, Ph. *Phys. Rev. B* **1998**, *57*, 2586.
(41) Charlier, J. C.; Ebbeson, T. W.; Lambin, Ph. *Phys. Rev. B* **1996**, *53*, 11108.
(42) Lambin, P.; Meunier, V.; Biro, L. P. *Carbon* **1998**, *36*, 701.
(43) Kane, C. L.; Mele, E. J. *Phys. Rev. B* **1999**, *59*, R12759.
(44) Lannoo, M.; Friedel, P. *Atomic and Electronic Structure of Surfaces*; Springer-Verlag: Berlin, 1991.
(45) Tamura, R.; Tsukada, M. *Phys. Rev. B* **1995**, *52*, 6015.
(46) Carroll, D. L.; Redlich, P.; Ajayan, P. M.; Charlier, J. C.; Blasé, X.; DeVita, A.; Car, R. *Phys. Rev. Lett*. **1997**, *78*, 2811.
(47) There are 56 cap possibilities for (13,−2). See ref 1.
(48) Bockrath, M.; Cobden, D. H.; McEuen, P. L.; Chopra, N. G.; Zettl, A.; Thess, A.; Smalley, R. E. *Science* **1997**, *275*, 1922.
(49) Tans, S. J.; Devoret, M. H.; Dai, H.; Thess, A.; Smalley, R. E.; Geerligs, L. J.; Dekker, C. *Nature* **1997**, *386*, 474.
(50) Venema, L. C.; Wildoer, J. W. G.; Temminck Tunistra, H. L. J.; Dekker, C.; Rinzler, A. G.; Smalley, R. E. *Appl. Phys. Lett*. **1997**, *71*, 2629.
(51) Odom, T. W.; Huang, J.-L.; Lieber, C. M., manuscript in preparation.
(52) Rubio, A.; Sanchez-Portal, D.; Attach, E.; Ordoejon, P.; Soler, J. M. *Phys. Rev. Lett*. **1999**, *82*, 3520.
(53) Bulusheva, L. G.; Okotrub, A. V.; Romanov, D. A.; Tomanek, D. *J. Phys. Chem. A* **1998**, *102*, 975.
(54) Rochefort, A.; Salahub, D. R.; Avouris, Ph. *J. Phys. Chem. B* **1999**, *103*, 641.
(55) Grabert, H.; Devort, M. H. *Single Charge Tunneling*; Plenum: New York, 1992.
(56) Odom, T. W.; Huang, J.-L.; Cheung, C.-L.; Lieber, C. M., submitted for publication.
(57) Hanna, A. E.; Tinkham, M. *Phys. Rev. B* **1991**, *44*, 5919. Ralph, D. C.; Black, C. T.; Tinkham, M. *Phys. Rev. Lett*. **1995**, *74*, 3241.
(58) Nayfeh, M. H.; Brussel, M. K. *Electricity and Magnetism*; John Wiley and Sons: New York, 1985.
(59) We estimate *d* assuming the finite-sized nanotubes are resting on a single layer of tubes, which is reasonable since the rope before cutting appeared "raft-like."